# Metasurface-Enhanced Raman Spectroscopy (mSERS) for Oriented Molecular Sensing

Yuan Zeng<sup>1,2</sup>, Riddhi Ananth<sup>3</sup>, Tyler J. Dill<sup>1</sup>, Andrea Rodarte<sup>1</sup>, Matthew J. Rozin<sup>1,2</sup>, Nathan Bradshaw<sup>1</sup>, Eric R. Brown<sup>1</sup>, and Andrea R. Tao<sup>1,2,3\*</sup>

<sup>1</sup>Department of NanoEngineering, University of California, San Diego, 9500 Gilman Drive MC 0448, La Jolla, California 92093-0448

<sup>2</sup>Materials Science and Engineering, University of California, San Diego, 9500 Gilman Drive, La Jolla, California 92093

<sup>3</sup> Department of Chemistry & Biochemistry, University of California, San Diego, 9500 Gilman Drive, La Jolla, California 92093

\*Email: atao@eng.ucsd.edu

### **Abstract:**

Surface-enhanced Raman spectroscopy (SERS) is a widely used sensing technique for ultra-sensitivity chemical sensing, biomedical detection and environmental analysis. Because SERS signal is proportional to the fourth power of the local electric field, several SERS applications have focused on the design of plasmonic nanogaps to take advantage of the extremely strong near-field enhancement that results from plasmonic coupling, but few designs have focused on how SERS detection is affected by molecular orientation within these nanogaps. Here, we demonstrate a nanoparticleon-metal metasurface designed for near-perfect optical absorption as a platform for Raman detection of highly-oriented molecular analytes, including two-dimensional materials and aromatic molecules. This metasurface platform overcomes challenges in nanoparticle aggregation, which commonly leads low or fluctuating Raman signals in other colloidal nanoparticle platforms. Our metasurface-enhanced Raman spectroscopy (mSERS) platform is based on a colloidal Langmuir-Blodgett film, with up to 32% surface coverage density of nanogaps across an entire sensor chip. In this work, we perform both simulations of the local electric field and experimental characterization of the mSERS signal obtained for oriented molecular layers. We then demonstrate this mSERS platform for the quantitative detection of drinking-water toxin, polybrominated diphenylether (BDE-15) with a limit of detection of 0.25 μM under 530 μW excitation. This detection limit is comparable to other SERS-based sensors operating at laser powers over three orders of magnitude higher, indicating the promise of our mSERS platform for non-destructive and low-level analyte detection.

**Keywords:** colloids, plasmonic, metasurface, chemical sensing, SERS,

### Introduction

Surface-enhanced Raman spectroscopy (SERS) is a well-developed surfacesensitive technique that relies on large enhancements — with a theoretical enhancement factor up to 10<sup>13</sup> and most experimental enhancement factors measuring between 10<sup>7</sup> to 10<sup>11</sup> 1,2 —of Raman scattering signals from chemisorbed or physiosorbed molecules near a metal surface.<sup>3,4</sup> The enhancement mechanism is mainly explained by two phenomena associated with electromagnetic and chemical charge transfer effects. In the first, the excitation of localized surface plasmon resonances (LSPRs) supports nanoscale localization of the electromagnetic near-field (i.e. the formation of hotspots), where enhancement factor is approximately proportional to the fourth power of this near-field intensity.<sup>4–6</sup> In the second mechanism, intermolecular charge transfer, charge transfer between a metallic surface and adsorbed molecules produces enhancements in Raman scattering due to resonance effects between the excitation of light and various electronic processes.<sup>7-9</sup> Decades of effort have been dedicated toward understanding and optimizing these two mechanisms for maximizing SERS signals for applications such as single-molecule sensing<sup>10,11</sup> and biomedical imaging.<sup>12</sup>

While SERS performed on rough metal surfaces has been used as a platform to provide signal enhancement for over forty years, <sup>13</sup> such substrates provide low hotspot uniformity, poor optical tunability in operation wavelength, and low surface sensitivities due to poor near-field confinement. In response, the past two decades has seen incredible growth of SERS substrates based on aggregated nanoparticles (NPs) that generate large field confinement due to plasmonic coupling between closely spaced NPs. <sup>10,14–17</sup> While aggregated NPs can provide large SERS signals and can provide a means toward large-scale fabrication of SERS platforms, the large sample-to-sample variation of these materials inherently limits the ability to perform quantitative SERS analysis of analyte concentration. For example, prior work measuring the distribution of SERS intensities for molecules adsorbed to a closed-packed Ag NP film showed that "cold" sites contain 61% of analyte molecules and that 24% of the total

observed SERS signal is given by less than 0.007% of the total analyte molecules located in hotpots with anomalously highest enhancement factors. This heterogeneity in signal collection over a single SERS substate creates challenges in utilizing these NP-based platforms for calculating sensing metrics such as limit of detection (LOD), where a clear dependence between SERS signal and molecular concentration must be established. In addition, the nanogaps responsible for hotspot formation in these NP aggregates are characterized by random orientations and morphologies, which limits the optimization of charge transfer processes that depend highly on molecular orientation within a nanogap.

In more recent years, the design of SERS platforms has focused on metallic substrates that utilize coupling between individual plasmonic NPs and metal films, such as nanoscale patch antenna (NPA) structures and metasurfaces comprised of nanoparticles deposited on top of metal substrates. 19,20 Yi et al. drop-casted a colloidal mixture of Rhodamine 6G (R6G) and Ag nanocubes (AgNCs) onto a polymer coated silver thin film and achieved 10<sup>-11</sup> M limit of detection for R6G molecules.<sup>21</sup> Marshall et al. used a spin coating method to deposit Ag nanospheres (AgNS) on a polymer-coated Ag thin-film. 22,23 The relative SERS intensity depends on the molecular orientation relative to the local electric field because SERS intensity is proportional to  $\cos^2(\theta)$ , where  $\theta$  is the angle between the local electric field and Raman tensor directions.<sup>24</sup> By modeling molecular geometry and local field directions in density functional theory calculations, they were able to calculate the molecular orientation of a trapped analyte. However, to avoid interparticle coupling stemming from disordered aggregation, both NPA structures typically have a very low surface density of NPs, precluding many of these SERS platforms from being employed in SERS mapping and quantitative analysis of large-scale analytes (e.g. molecular monolayers or two-dimensional materials).

To address these challenges with molecular orientation and large-scale SERS mapping, we fabricated colloidal metasurfaces using a previously published method<sup>25</sup>

using AgNCs that are deposited onto a flat metal film.<sup>26–28</sup> The resulting metasurface-based surface-enhanced Raman spectroscopy (mSERS) substrate possess a "nanocube-on-metal" (NOM) type structure and operate by confining light to a resonant optical gap,<sup>27</sup> where a molecular analyte is trapped. Advantageously, Raman enhancement can be generated from a large cross-sectional area (>20% of the total substrate area) of the mSERS substrate,<sup>26</sup> which allows for sampling a broad range of different analytes without necessitating specific binding chemistries. Here, we characterize these mSERS substrates and the design parameters that dictate mSERS detection capabilities at low analyte concentrations, such as nanocrystal density, illumination wavelength, near-field polarization, and molecular analyte orientation. As a demonstration, we carry out sensing experiments for an emerging organic pollutant in drinking water, Bis (4-bromophenyl) ether (BDE-15) that is expected to possess highly anisotropic molecular orientations when adsorbed onto a surface. We measure the quantitative LOD for BDE-15 in aqueous solutions to compare to other SERS-based PBDE sensors.<sup>29</sup>

# **Results and Discussion**

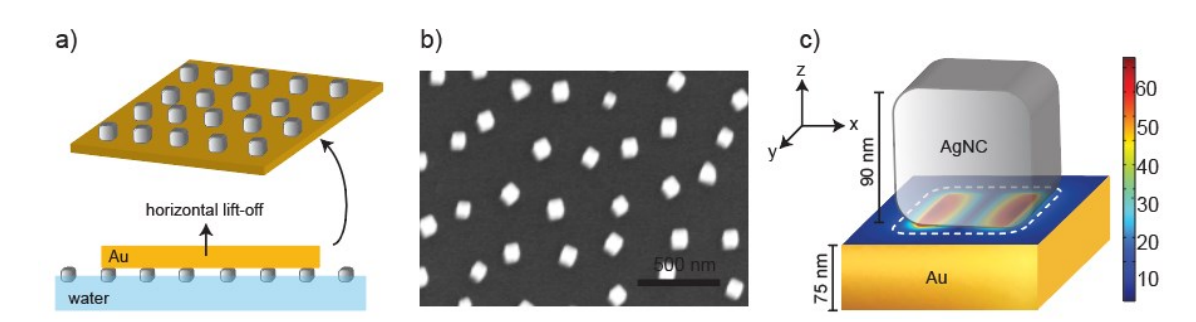


**Figure 1 | Fabrication of the mSERS platform: (a)** Schematic of the colloidal metasurface via deposition of AgNCs onto a flat Au film. **(b)** Top-down SEM image of the resulting metasurface showing well-spaced AgNCs (90 nm in edge length). **(c)** Schematic of a single nanocube-on-metal (NOM) meta-atom and the location of the electromagnetic hotspot inside the meta-atom gap. The color map shows FDTD simulation results indicating the overall electric field strength associated with the optical gap.

A schematic of the fabrication process for our NOM metasurface is shown in Figure 1a, depicting how Langmuir-Blodgett deposition is used to generate the layered metallic structure.<sup>28</sup> Briefly, Ag nanocubes (AgNCs) are dispersed in chloroform, drop-

casted onto an air-water interface to form a floating AgNC monolayer, and isothermally compressed with a mechanical barrier until a target AgNC density within the monolayer is reached. Here, we aim for a target AgNC density range of 5-30% surface coverage, which avoids the formation of AgNC clusters or close-packing within the monolayer. The AgNC monolayer is then transferred to an Au thin-film by horizontal dip-coating. This bottom-up assembly technique allows us to form a NOM metasurface with controlled AgNC densities in the range of 11-65 AgNCs / µm² such that the AgNCs that behave as well-separated optical meta-atoms (Fig. 1b). Figure 1c shows a finitedifference time-domain (FDTD) model and electromagnetic heat map for a single metaatom consisting of AgNCs (edge length=90 nm, edge/corner radius of curvature=10 nm) and a 75 nm thick Au thin-film separated by a dielectric gap of 6 nm. In this model, the dielectric gap is modeled to approximate the polymer layer that serves as the capping agent in the AgNC synthesis and is retained on the AgNC surface. Strong capacitive coupling between the AgNC and Au thin-film in this meta-atom produces an electromagnetic hot-spot located inside the dielectric gap that gives rise to a 70-fold near-field enhancement (E/E<sub>0</sub>) within the optical gap at the resonant wavelength of 847 nm (Supporting Information S1). This heat map includes both the in-plane polarized electric field components (Ex, Ey) and the out-of-plane polarized electric field component Ez, with the highest intensity near-field generated from the Ez component.

First, we investigated how meta-atom density affects mSERS intensity. We selected the widely used Raman analyte benzenethiol (BT) <sup>30–32</sup> as a SERS benchmark for our analysis because it is known to form an oriented, uniform self-assembled monolayer (SAM) on metal surfaces<sup>33</sup> and because the SERS fingerprint of BT adsorbed on a metal surface is identical to that of free BT molecules in solution.<sup>34</sup> We deposited AgNCs (edge length=91 ± 4 nm) on a BT functionalized Au thin-film with an AgNC density estimated by SEM at the following surface coverages: 6%, 16%, 17%, 27%, 32%, 43%, and 65%. Figure 2a shows averaged mSERS spectra for these various surface coverages, where each spectral point is an average of 100 points collected over the metasurface. The peaks at 999 cm<sup>-1</sup> and 1076 cm<sup>-1</sup> correspond to

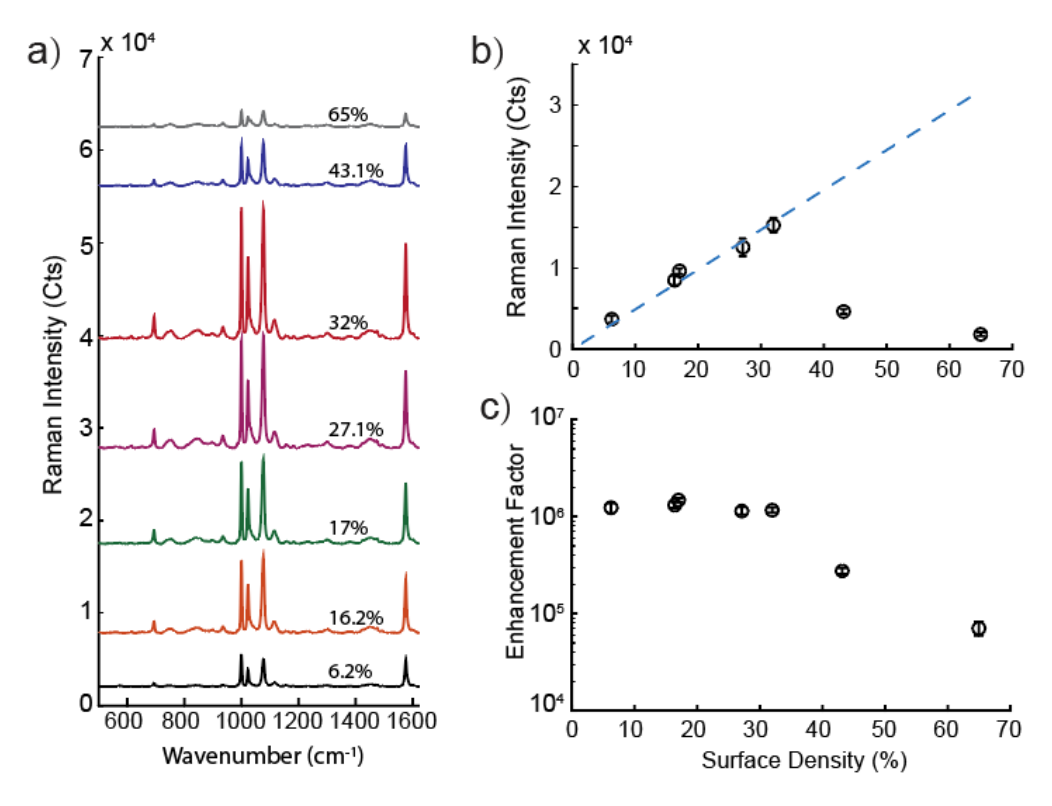


**Figure 2 | mSERS intensity and enhancement factor: (a)** Raman Spectra for BT collected using our mSERS platform as a function of increasing meta-atom density. **(b)** Raman intensity of the 1023 cm<sup>-1</sup> vibrational mode of BT as a function of meta-atom density. **(c)** Calculated meta-atom density dependent enhancement factor (EF) showing a falloff as AgNCs begin to aggregate at higher surface densities.

the  $\beta_{\rm CCC}(a_1)$  vibrational mode, the peak at 1023 cm<sup>-1</sup> corresponds to  $\beta_{\rm CH}(a_1)$  vibrational mode and the peak at 1575 cm<sup>-1</sup> corresponds to C=S ring stretch  $(a_1)$  mode.<sup>35</sup> As coverage density increases from 6% to 32%, the mSERS intensity of all the peaks gradually increases. However, when coverage density increases above 32%, the mSERS intensity starts to decrease. We plotted the intensity of the  $\beta_{\rm CH}(a_1)$  vibrational mode (1023 cm<sup>-1</sup>) for each coverage density (Figure 2b). As coverage density increases from 6% to 32%, the SERS intensity increases linearly (R<sup>2</sup> = 0.96) from 1950 to 9492 counts. At 43% and 65% coverage density, the average cluster size is 2 AgNCs and 56 aggregated AgNCs, respectively, resulting in a significant decrease in SERS intensity to 3015 and 1150 counts, respectively. Figure 2c shows the calculated change in SERS enhancement factor (EF) using the procedure reported by Zhang et al.<sup>36</sup> As coverage density increases from 6% to 32%, the EF stays constant at 10<sup>6</sup>, indicating that near-field intensity is independent of coverage density when meta-atoms are well

spaced. However, when coverage density increases from 32% to 65%, the EF decreases by more than one order of magnitude. This EF decrease is attributed to interparticle coupling between neighboring AgNCs, which causes a redshift of the optical resonance and causes the metasurface to move off-resonance at our laser wavelength (785 nm).<sup>28</sup>

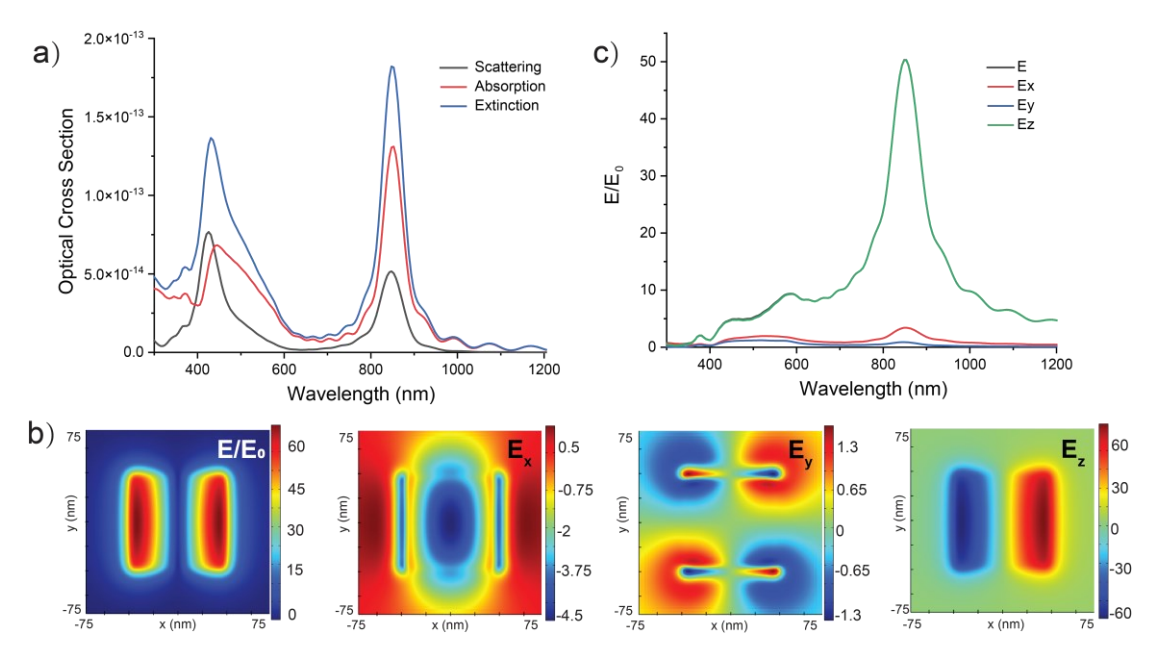


**Figure 3 | Simulated far-field spectra, near-field distributions, and EFs**: a) Simulated optical scattering (black), absorption (red) and extinction spectra (blue). b) Color map showing the simulated electric field distribution for different polarizations at the nanogap resonance. From left to right: E/E<sub>0</sub>, x-polarized E-field, z-polarized E-field, and they-polarized E-field. (c) Wavelength-dependent E-field with different polarizations. The black line (E/E<sub>0</sub>) overlaps significantly with the green line and is not visible in this plot.

Because SERS enhancement is known to exhibit a strong polarization dependence that is dictated by the geometries of the metal nanostructures used as substrates, <sup>37–39</sup> we carried out a wavelength-dependent simulation of both in-plane (E<sub>x</sub>, E<sub>y</sub>) and out-of-plane (E<sub>z</sub>) components of the near-field to calculate the theoretical contribution of each component to the mSERS enhancement factor in Fig. 2c. Figure 3a shows a simulated far-field spectra of our NOM metasurface. At 425 nm, there is a large scattering cross-section peak and a broad absorption cross-section peak originating from a cube mode resonance. <sup>27</sup> At 847 nm, the gap mode resonance results

in a strong absorption cross-section and moderate scattering cross-section, which can provide enhancement for both excitation and emission processes of mSERS. Figure 3b shows a color map of the electric field distribution for illumination at the gap mode resonance wavelength, 847 nm. This on-resonance gap mode is a dipolar mode with a maximum enhancement of  $E/E_0$  =71. Also, this gap mode resonance is highly polarized. The  $E_x$  component of near-field enhancement is 4.5, the  $E_y$  component is 1.3 and the  $E_z$  component is 66, indicating that the out-of-plane ( $E_z$ ) polarized electric-field is dominant in our metasurface. We then integrated the electric field strength over the hot spot area for each wavelength, as plotted in Figure 3c. At the gap mode resonance (847 nm), the  $E_z$  component is more than 2 orders of magnitude higher than the  $E_x$  and  $E_y$  components. At the cube mode resonance (425 nm), this NOM structure has a large scattering cross-section, but the near-field enhancement is much weaker than the gap mode resonance.

The large out-of-plane component of the near-field suggests that molecular orientation is likely to play a large role in determining the Raman EF of our NOM metasurface when detecting analytes that are highly anisotropic and that adopt preferred orientations within the optical gap. To better quantify the relationship between molecular analyte orientation and the EF of our NOM metasurface, we characterized our mSERS response using two different analytes that adopt different orientations within the NOM gap: BT and pyrene. Figure 4a shows a schematic of these two analyte orientations. Owing to  $\pi$ - $\pi$  interactions between aromatic rings, BT molecules preferentially orientate normal to the metal surface and self-organize in this manner 40. On the other hand, because the transition dipoles of pyrene are in-plane polarized, pyrene molecules preferentially orient parallel to the metal surface. 41 Figure 4b shows a comparison of the Raman spectra obtained for isotropic BT molecules dispersed in ethanol (black line), the bare NOM metasurface prior to BT exposure (blue line), and the NOM metasurface after exposure to BT (red line). The BT-NOM exhibits peaks corresponding to the  $\beta_{CCC}(a_1)$  vibrational mode at 999 cm<sup>-1</sup>,  $\beta_{CH}(a_1)$  vibrational mode at 1023 cm<sup>-1</sup> and  $\beta_{CCC}(a_1)$  vibrational mode at 1076 cm<sup>-1</sup>. Compared to the Raman spectra of free BT molecules, the vibrational modes at 999 cm<sup>-1</sup> and 1023 cm<sup>-1</sup> are redshifted

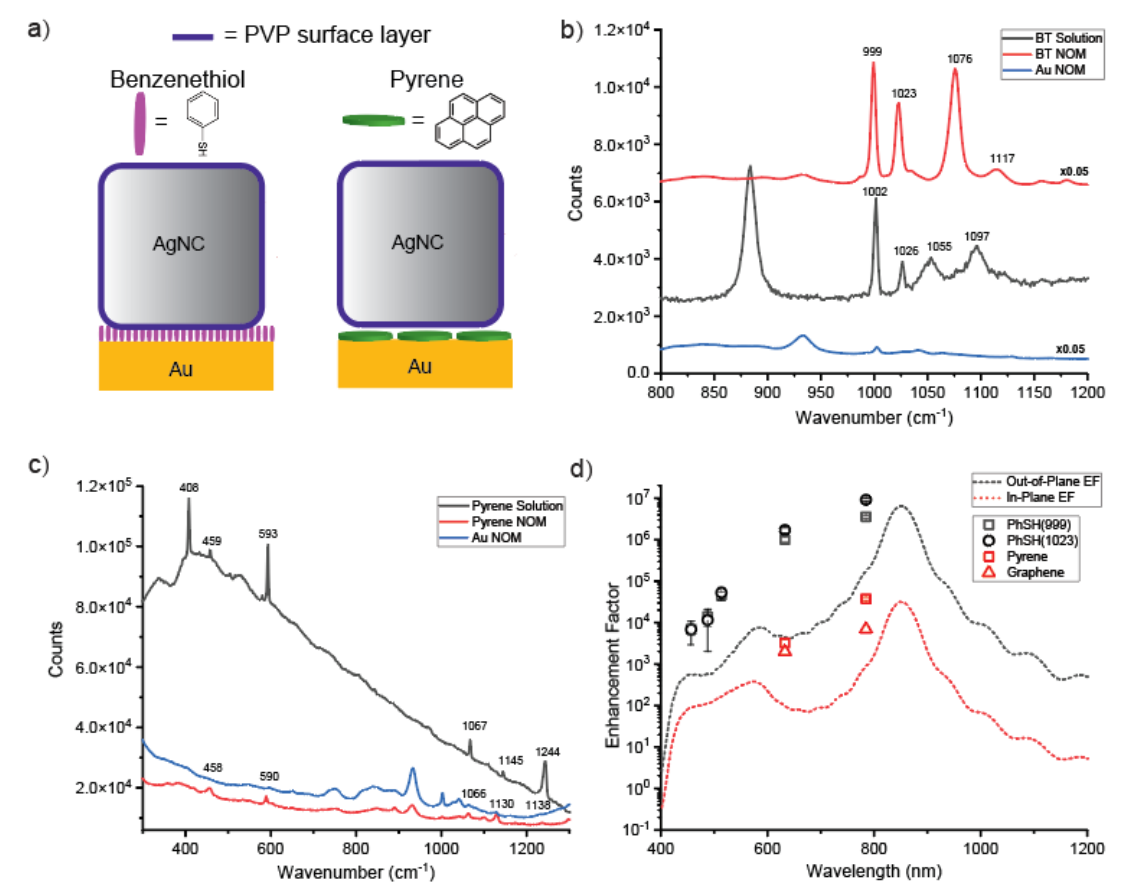


**Figure 4** | **Schematic and wavelength dependent EF of molecule analyst: (a)** Schematic of meta-atom with BT molecules (left) and pyrene molecules (right) in gap. **(b)** Raman spectra of BT-NOM under 785 nm excitation (black is free BT molecules in Ethanol, red is BT metasurface and blue is metasurface without BT). **(c)** Raman spectra of pyrene metasurface under 785 nm excitation (black is free pyrene molecules in Ethanol, red is pyrene metasurface and blue is metasurface without pyrene). **(d)** wavelength dependent EF for BT metasurface (black square is BT vibrational mode at 999 cm<sup>-1</sup>, black circle = 1023 cm<sup>-1</sup>), pyrene metasurface (red square = 590 cm<sup>-1</sup>) and graphene metasurface (red triangle = 2593 cm<sup>-1</sup>).

~3 cm<sup>-1</sup> which is attributed to surface adsorption. However, the vibrational mode at 1076 cm<sup>-1</sup> is redshifted ~15 cm<sup>-1</sup>,which overlaps with the ethanol C-H rocking mode at 1096 cm<sup>-1</sup>.<sup>35,42</sup> In addition, the peak at 884 cm<sup>-1</sup> can be assigned to the ethanol C-C stretching mode and the peak at 1055 cm<sup>-1</sup> corresponds to the ethanol C-O stretching mode (Supporting Information S2).<sup>42</sup> Figure 4c shows the Raman spectra of pyrene dispersed in ethanol (black line) and pyrene adsorbed to the NOM metasurface (red line). Because pyrene is an excimer with strong fluorescence, the pyrene solution has a broad band background centered around 450 cm<sup>-1</sup>.<sup>43,44</sup> The Raman peaks at 408 cm<sup>-1</sup>, 458 cm<sup>-1</sup> and 593 cm<sup>-1</sup> correspond to skeletal stretching modes, the peaks at 1067 cm<sup>-1</sup> and 1145 cm<sup>-1</sup> correspond to C-H in-plane bending and the peak at 1244 cm<sup>-1</sup>

corresponds to C-C stretching/C-H in-plane bending.<sup>45</sup> Compared with the pyrene solution, the pyrene NOM signature only has two detectable peaks at 458 cm<sup>-1</sup> and 593 cm<sup>-1</sup>. The pyrene band at 408 cm<sup>-1</sup> is notably weaker when adsorbed to the NOM, which is likely due to charge transfer with the Au thin-film. This is also supported by the observed fluorescence quenching in the pyrene-NOM spectrum.

We then calculated EF using the fourth-power approximation where EF =  $(E/E_0)^4$  where  $E/E_0$  is the local electric field.<sup>4,5</sup>. Because our NOM metasurface has a polarized E-field which dominated by  $E_z$  and because our surface analytes are highly oriented, we modified this fourth-power equation with an additional dipole moment term, as follows:<sup>22</sup>

$$G = \frac{|E(\omega_0)|^2}{|E_0(\omega_0)|^2} \left( \frac{\left| \hat{E} \cdot \hat{\mu} \right|^2}{\left| \widehat{E_0} \cdot \hat{\mu} \right|^2} \right) \frac{\rho(\omega_1)}{\rho_0(\omega_1)} = G_{ex} \cdot S_{\mu} \cdot G_{em}$$

Where  $E_0$  is the incident electric field, E is the electric field at molecule location,  $\omega_0$  is incident frequency,  $\omega_1$  is scattering frequency,  $\widehat{E_0}$  and  $\widehat{E}$  correspond to polarization direction of incident electric field and electric field at the molecule location,  $\widehat{\mu}$  corresponds to the oriented molecular dipole, and  $\rho$  corresponds to optical density. Because both  $\widehat{E}$  and  $\widehat{\mu}$  have x-, y-, and z-components,  $|\widehat{E} \cdot \widehat{\mu}|^2$  can be rewritten as  $(E_x \mu_x)^2 + (E_y \mu_y)^2 + (E_z \mu_z)^2$  where  $(E_x \mu_x)^2 + (E_y \mu_y)^2$  is an in-plane term and  $(E_z \mu_z)^2$  is an out-of-plane term.

Figure 4d shows the calculated and experimental wavelength-dependent Raman EFs for the BT-NOM and pyrene-NOM samples. Calculated EFs are obtained from the FDTD-simulated near-field strengths for the out-of-plane (Ez, black dashed line) and in-plane (Exy, red dashed line) polarized components. At resonance, the in-plane oriented dipole moments are enhanced by more than 4-orders of magnitude and the out-of-plane oriented dipole moments are enhanced by more than 6-orders of magnitude. Experimental EFs were obtained by measuring mSERS intensities for the BT-NOM and pyrene-NOM at five different Raman excitation wavelengths: 457 nm,

488 nm, 514 nm, 633 nm and 785 nm. We then used the strongest Raman bands (the 999 cm<sup>-1</sup> and 1023 cm<sup>-1</sup> peaks for BT and the 593 cm<sup>-1</sup> peak for pyrene) to calculate the experimental EFs. In the BT-NOM, the experimental EFs are one order of magnitude higher than the calculated EFs at 457 nm, 488 nm, 514 nm and 785 nm. This is attributed to chemical contributions<sup>46-48</sup> to SERS enhancement. At 633 nm excitation, the experimental EF is more than two orders of magnitude higher than calculated EF. This large overperformance likely originates from a number of factors: i) partially on-resonance meta-atoms in our metasurface due to the size distribution of AqNCs, ii) the areal distribution of NOM junctions, and iii) resonant transitions attributed to mixed metal-molecular electronic states that are known to give rise to additional two orders of magnitude in SERS enhancement<sup>46</sup>. Also, we observed that the EF of the β<sub>CH</sub>(a<sub>1</sub>) vibrational mode (1023 cm<sup>-1</sup>) is 2.58-fold larger than the EF of the β<sub>CCC</sub>(a<sub>1</sub>) vibrational mode (999 cm<sup>-1</sup>) at resonance. This difference in EF originates from the difference in dipole moment orientation, given that  $\beta_{CH}(a_1)$  has larger  $\mu_z$ component than  $\beta_{CCC}(a_1)$ . At off-resonance wavelengths, near-field enhancement does not play a dominant role and there is no difference between these two EFs for  $\beta_{CH}(a_1)$ and  $\beta_{CCC}(a_1)$ .

In the pyrene-NOM, we only have two data points at 633 nm and 785 nm because pyrene has a lower Raman scattering cross-section and its experimental EF at 457 nm, 488 nm and 514 nm is lower than our instrumental detection limit (around 10³). The theoretical EF is calculated using the in-plane polarized near-field (red dashes). Overall, the experimental EF of the pyrene-NOM is more than two orders of magnitude lower than the experimental EF of the BT-NOM, indicating that pyrene molecules are enhanced by the relative weakly in-plane polarized near-field. Similar to the BT-NOM, the pyrene-NOM also exhibits a discrepancy of ~10 between experimental data and

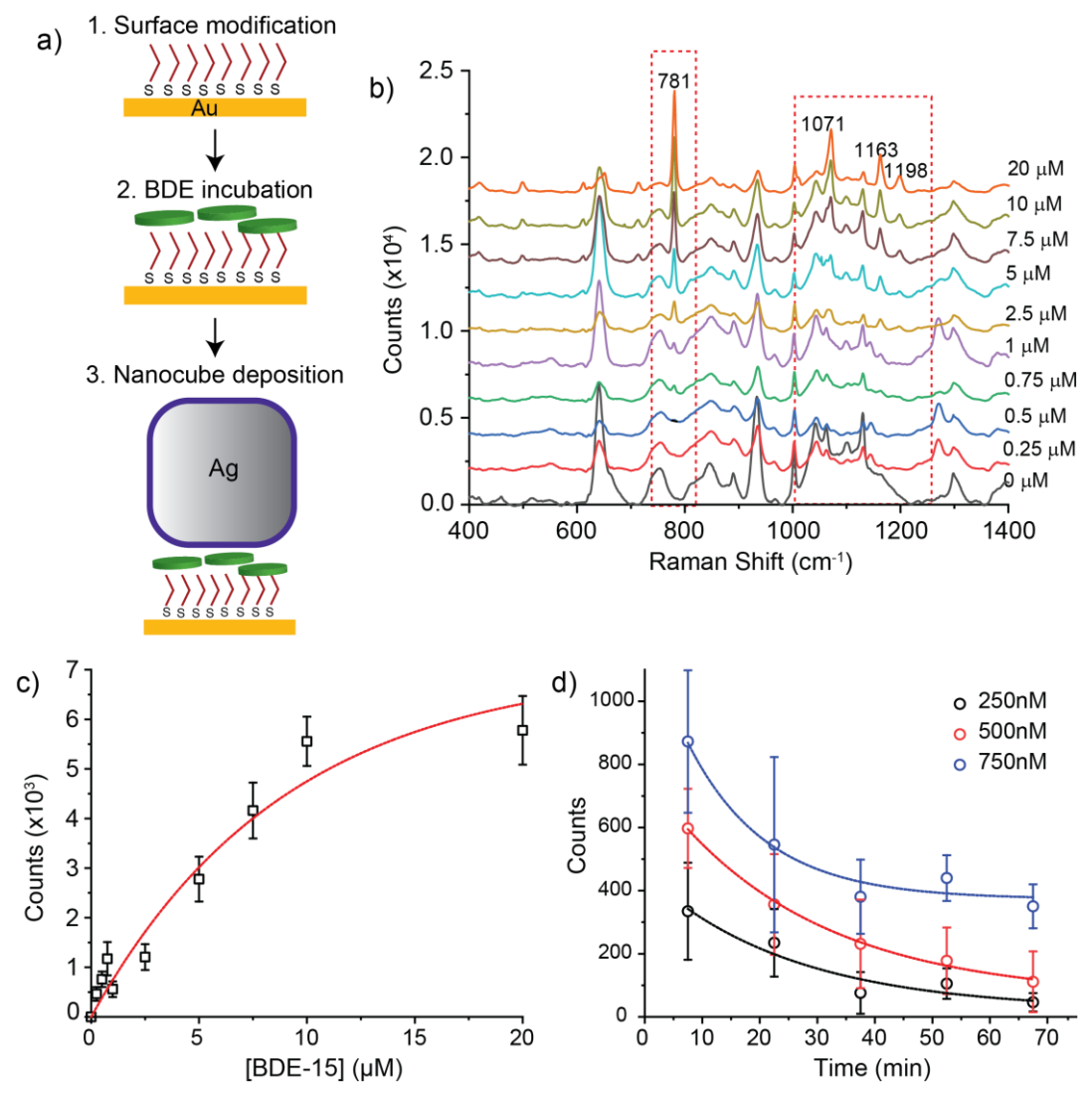


**Figure 5 | Schematic of PBDE mSERS sensor fabrication and Raman spectra of PBDE metasurface: (a)** Schematic of PBDE mSERS fabrication. (b) mSERS spectra of metasurface sensor incubated in different BDE-15 concentration (c) Concentration-dependent and (d) post-fabrication time-dependent Raman intensity of BDE-15 collected at 781cm<sup>-1</sup>.

simulated EF values. To confirm weaker enhancement for in-plane orientated molecules, we replaced pyrene molecules with monolayer graphene (Graphene-NOM) and the experimental EF is consistent with the calculated EF at 785 nm excitation. At 633 nm, there is a small overestimation in the experimental EF owing to both heterogeneities in AgNC size and shape defects.<sup>49</sup> The experimental EF of the pyrene-NOM is slightly higher than the Graphene-NOM which we attribute to trace amounts of misaligned pyrene molecules and molecular aggregation, leading to molecules that possess an out-of-plane orientation and, thus, a larger  $\mu_z$ .

Because our NOM structure provides an EF greater than four orders of magnitude for flat aromatic hydrocarbon molecules such as pyrene, it suggests that such a sensor platform might perform exceptionally well for in detecting hazardous analytes with similar planar molecular structures, such as BDEs. To demonstrate, we prepared a BDE mSERS sensor using the fabrication method shown in Figure 5a. First, a piranha-cleaned Au thin-film was functionalized with ethanethiol and incubated in a 1 μM BDE-15 solution. BDE-15 molecules spontaneously physisorb to the functionalized Au thin-film due to poor solubility of BDE-15 in water and due to attractive hydrophobic interactions between BDE-15 molecules and the alkyl chains of ethanethiol. Following this incubation, we transferred AqNCs to the functionalized Au thin-film via Langmuir-Blodgett deposition, trapping the physisorbed BDE-15 molecules inside a NOM junction. mSERS spectra were obtained by generating a Raman map with automated collection using a programmed x-y stage. Each mSERS spectrum obtained is the averaged lineshape from 49 different collection points (a 7x7 array) across the mSERS substrate. This averaging allows us to obtain highly reproducible mSERS signatures over thousands of meta-atoms. Figure 5b shows the mSERS spectra of our BDE sensor incubated at different BDE-15 concentrations. The peak at 781 cm<sup>-1</sup> corresponds to the β(C-H) mode, the peak at 1071 cm<sup>-1</sup> corresponds to the υ(C-Br), ring stretch mode, and the peaks at 1163 cm<sup>-1</sup> and 1198 cm<sup>-1</sup> correspond to the  $v_s$  (C-O),  $\beta$  (C-H) modes.<sup>50</sup> Although the peaks at 781 cm<sup>-1</sup>, 1071 cm<sup>-1</sup> and 1163 cm<sup>-1</sup> have similar intensities in the BDE-15 powder reference spectrum (Supporting Information S3), the peak at 781 cm<sup>-1</sup> has a higher relative intensity in our BDE mSERS sensor owing to stronger enhancement of the  $\beta(C-H)$  mode. This is attributed to symmetry-breaking upon BDE-15 adsorption to the mSERS substrate and the larger  $\mu_z$  component in  $\beta$ (C-H) dipole moment. At concentrations from 0  $\mu$ M to 0.25  $\mu$ M, no BDE-15 peak is apparent in the mSERS spectra because the BDE-15 concentration is lower than the limit of detection (LOD) of the platform. Above 0.25 µM, the peak intensity of the  $\beta(C-H)$  mode (781 cm<sup>-1</sup>) gradually increases with concentration; however, owing to strong background noise (1000 cm<sup>-1</sup> to 1200 cm<sup>-1</sup>) from polyvinylpyrrolidone (PVP) on the AgNCs, the peaks at 1071 cm<sup>-1</sup> and 1163 cm<sup>-1</sup> are

not detectable at concentrations below 2.5  $\mu$ M. As BDE-15 concentration is increased to above 2.5  $\mu$ M, three BDE-15 vibrational modes appear at 781 cm<sup>-1</sup>, 1071 cm<sup>-1</sup> and 1163 cm<sup>-1</sup>. This is consistent with the BDE-15 powder spectrum, although the peak maxima are slightly shifted by ~5 cm<sup>-1</sup>.

Moving forward, we chose to analyze the response of the 781 cm<sup>-1</sup> peak (β C-H mode) for quantitative BDE-15 analysis, aligned with previous studies.<sup>29</sup> Figure 5c shows the plot of mSERS intensity vs. BDE-15 concentration, it has a linear relation below 5 µM and decreases above 5 µM. This decreased detection at higher concentration ranges is indicative of: i) saturation of surface binding sites on Au substrate, ii) increased thickness in the adsorbed BDE-15 layer, which results in a larger gap distance and weaker near-field enhancement, and iii) increased surface roughness due to adsorbed BDE-15 causing a decrease in AgNC density. We performed a time-dependent study of the response of the BDE sensor to probe how robust the mSERS signal is. We observed a decrease in mSERS intensity with time, as plotted in Figure 5d which displays Raman counts at various times after AqNC transfer. At 7.5 min, 0.25 µM sensor has 334 counts, 0.5 µM sensor has 597 counts and 0.75 µM sensor has 873 counts. As post-fabrication time increases from 7.5 min to 67.5 min, the Raman intensity decreases exponentially to 46 counts, 111 counts and 350 counts, respectively. We attribute this exponential decay to molecular diffusion of analytes inside the nanogap, which has been previously observed 23,51,52 and likely to occur given that the mSERS hotspot is located less than 10 nm away from the edge of the nanogap. While this molecular diffusion potentially results in an underestimation of the LOD for our mSERS sensor, it provides added challenges in carrying out in-line quantitative analysis due to this time-dependent Raman signal, which will depend on both analyte diffusion timescales and the kinetics of analyte adsorption.

# Conclusion

Overall, we show that a colloidal NOM metasurface with a strong gap mode resonance can serve as a valuable platform for chemical detection based on mSERS.

Both FDTD simulations and experimental results confirm that the strong out-of-plane polarized near-field plays the dominant role in mSERS enhancement, providing ~10<sup>7</sup> enhancement for the out-of-plane and ~105 enhancement for the in-plane aligned aromatic molecules observed in this study. Because vibrational modes with different dipole moment orientations provide vastly different mSERS signal intensities, this platform provides the ability to study molecular orientation and local order/orientation of 2D materials and thin-films. As a chemical sensor for aromatic BDE-15 analytes, we achieved quantitative and reproducible measurements at low-level concentrations with a LOD of 0.25 µM. Although our metasurface has relative low maximum EF (10<sup>7</sup>), the large hotspot area of the AgNC meta-atom provides sampling over many more molecules and leads to a comparable LOD as other SERS-based BDE sensors that rely on only a few, high-performing hotspots. In the future, by decreasing meta-atom gap distance and precise engineering of the metasurface resonance frequency, the EF of this mSERS platform has the potential to exhibit even lower LODs in chemical sensing. Future work will focus on how such mSERS platforms can be utilized for in situ or in-line chemical sensing, where directional diffusion of physiosorbed molecules inside the gap will be addressed, in addition to improving mSERS performance and signal stability.

## Method

**Materials.** Ethanethiol (97%), Thiophenol (97%) were purchased from Sigma-Aldrich. Pyrene (in solution), SPEX CertiPrep (1.2 mL, 1000 μg / mL) was purchased from Fisher scientific. Pyrene (powder) was purchased from Spectrum Chemical. Bis(4-bromophenyyl) ether (BDE-15), 99% was purchased from Alfa Aesar. Monolayer graphene on pre-diced Au substrate (1cm x 1 cm) was ordered from Grolltex, Inc. All materials were used as purchased.

**Gold Substrate Fabrication**. Au thin-film substrates were fabricated through Sputter Deposition (using Denton Discovery 18 Sputter System). 100mm diameter, 500 µm thick P type doped wafer (University wafer) was cleaned with isopropanol and cleanroom cloth. The sputtering RF bias is used to clean the substrate for 20 seconds

and followed with 10 seconds Cr (400 W) and 120 seconds Au (300 W) sputtering with the Ar gas pressure as 2.4 mTorr. Then the wafer was diced into 1cm x 1cm size for later use.

BT SAM Substrate Fabrication. Au thin-film substrates were washed with ethanol, piranha solution (60 seconds), DI water and dried with compressed air. Then the washed substrates were incubated in 1mL, 10% BT solution (in Ethanol) for 3 hours, rinsed 8 times with ethanol thoroughly, dried under compressed air and kept in a fume hood overnight (about 16 hours).

**Pyrene SAM Substrate Fabrication**. 2mL, 5  $\mu g$  / mL pyrene solution (in chloroform) was deposited dropwise onto a deionized water (18  $M\Omega$ ) subphase in KSV Nima KN2001 Langmuir-Blodgett trough. Then the Teflon barriers were compressed at 4 mm / min speed until the end and achieved 10mN  $\pm$  1mN surface pressure (surface area is about 30 cm²). Pre-cleaned Au thin-film substrate was mechanically dipped into the air-water interface quickly, placed vertically on paper towel and dried in air.

Ag nanocubes (AgNCs) Preparation. Ag Nanocubes were synthesized via a polyol method published elsewhere.<sup>53</sup> AgNO<sub>3</sub> is reduced in a solution of pentanediol, CuCl<sub>2</sub>, and polyvinylpyrrolidone (PVP) (M<sub>w</sub>=55,000). PVP serves as a selective capping agent that controls nanocube nucleation and growth. The reaction was allowed to proceed until the resulting colloidal dispersion turned an opaque yellow-green color. To remove excess reactants, the nanocube dispersion product was centrifuged (2700 rpm for 10 min) using a Thermo Scientific CL2 Centrifuge, and the resulting precipitate was redispersed and diluted in an ethanol and water mixture, and then vacuum-filtered (Millipore Durapore membranes, with 0.65 μm, 0.45 μm, then 0.22 μm pore sizes) to remove any larger, unwanted particles.

**Metasurface Fabrication**. To prepare the AgNCs for Langmuir-Blodgett deposition, a nanocube dispersion is washed by centrifugation and the precipitate is dispersed in EtOH. This process was repeated three times before finally dispersing the precipitate in chloroform. AgNC films were fabricated using a KSV Nima KN2001 Langmuir-Blodgett trough, as previously described.<sup>54</sup> The AgNC solution was deposited drop-wise onto a deionized water (18  $M\Omega$ ) subphase. The film formed at the

air-water interface was allowed to equilibrate for 30 min. The Ag nanocube film was isothermally compressed to a desired surface density before being transferred to the Au or functionalized Au substrates via mechanical dipping.

PBDE mSERS Sensor Fabrication. Pre-cleaned Au thin-film substrate was incubated in 1mL, 1% Ethanethiol solution (in Ethanol) for 3 hours. Washed with Ethanol 5 times and dried under compressed air. Then the substrates were held in a glass vial with 10 mL BDE-15 DI water solution (prepared by diluting 0.1mM BDE-15 ethanol solution with DI water), stirring at 500 RPMs and keep 3 hours. Because the surface is hydrophobic, there was no water residue left on the Au thin-film substrate with the BDE-15 molecules. Then AgNCs were deposited on the thin-film with the method introduced before.

mSERS measurements. All Raman spectra were obtained using a Renishaw inVia confocal Raman microscope. Measurements were taken at powers < 1 mW to prevent laser induced damage. 785 nm illumination was provided by a Renishaw 300 mW diode laser. 633 nm illumination was provided by a Renishaw 17mW HeNe laser. 514, 488, and 457 nm illumination was provided by a Modu-Laser 50 mW Ar+ Ion laser. All spectra were collected through a 50x, 0.9 NA objective.

with Lumerical FDTD Solutions. AgNCs (Palik dielectric data) were modeled in 90 nm cube size, 10 nm radius of curvature on the corners with an underlying 75 nm Au thin-film. A 6 nm dielectric layer with n = 1.4 was added to reflect the analyte layer positioned within the plasmon volume. Incident light was injected normal to the substrate and polarized parallel to the (100) faces of the AgNC. A 1 nm global mesh was used; to improve accuracy, the mesh size was reduced in the gap region to 0.5 nm. The electric field profiles were calculated in the plane of the Au thin film, 1 nm offset from the surface. An average EF for the mSERS substrate is calculated by summing  $|E/E_o|^4$  at each pixel (1x1 nm) and normalizing to the cross-sectional area of each nanocubes. This calculation was carried out at discrete wavelengths over the visible range.

# Acknowledgements

The authors would like to thank Nano3 and the San Diego Nanotechnology Infrastructure (NSF Award ECCS-2025752), the UC San Diego MRSEC (NSF Award DMR-2011924), and the NanoEngineering MRC for use of their equipment and facilities, and Dr. Aliaksandr Zaretski of Grolltex, Inc. for graphene samples and graphene fabrication. This work was sponsored in part by the UC San Diego Materials Research Science and Engineering Center (UC San Diego MRSEC), supported by the National Science Foundation (Grant DMR-2011924) and in part by the National Science Foundation Grant CHE-1807891.

### References:

- Lee, D. & Yoon, S. Effect of Nanogap Curvature on SERS: A Finite-Difference Time-Domain Study. J. Phys. Chem. C 120, 20642–20650 (2016).
- Le Ru, E. C., Blackie, E., Meyer, M. & Etchegoint, P. G. Surface enhanced raman scattering enhancement factors: A comprehensive study. *J. Phys. Chem.* C 111, 13794–13803 (2007).
- Jeanmaire, D. L. & Van Duyne, R. P. Surface raman spectroelectrochemistry.
  Part I. Heterocyclic, aromatic, and aliphatic amines adsorbed on the anodized silver electrode. *J. Electroanal. Chem.* 84, 1–20 (1977).
- 4. Sharma, B., Frontiera, R. R., Henry, A. I., Ringe, E. & Van Duyne, R. P. SERS: Materials, applications, and the future. *Materials Today* vol. 15 16–25 (2012).
- 5. Stiles, P. L., Dieringer, J. A., Shah, N. C. & Van Duyne, R. P. Surface-Enhanced Raman Spectroscopy. *Annu. Rev. Anal. Chem.* **1**, 601–626 (2008).
- Schatz, G. C., Young, M. A. & Duyne, R. P. Electromagnetic Mechanism of SERS. in *Surface-Enhanced Raman Scattering* 19–45 (Springer Berlin Heidelberg, 2006). doi:10.1007/3-540-33567-6\_2.
- 7. Wang, Y. et al. Exploring the effect of intermolecular H-bonding: A study on charge-transfer contribution to surface-enhanced Raman scattering of p-mercaptobenzoic acid. J. Phys. Chem. C 118, 10191–10197 (2014).

- 8. Liu, S., Wan, S., Chen, M. & Sun, M. Theoretical study on SERRS of rhodamine 6G adsorbed on Ag2 cluster: Chemical mechanism via intermolecular or intramolecular charge transfer. *J. Raman Spectrosc.* **39**, 1170–1177 (2008).
- 9. Ling, X., Moura, L. G., Pimenta, M. A. & Zhang, J. Charge-transfer mechanism in graphene-enhanced Raman scattering. *J. Phys. Chem. C* **116**, 25112–25118 (2012).
- Lim, D. K., Jeon, K. S., Kim, H. M., Nam, J. M. & Suh, Y. D. Nanogapengineerable raman-active nanodumbbells for single-molecule detection. *Nat. Mater.* 9, 60–67 (2010).
- Blackie, E. J., Le Ru, E. C. & Etchegoin, P. G. Single-molecule surface-enhanced raman spectroscopy of nonresonant molecules. *J. Am. Chem. Soc.* 131, 14466–14472 (2009).
- Kong, K. V., Lam, Z., Goh, W. D., Leong, W. K. & Olivo, M. Metal carbonyl-gold nanoparticle conjugates for live-cell SERS imaging. *Angew. Chemie Int. Ed.* 9796–9799 (2012).
- 13. Fleischmann, M., Hendra, P. J. & McQuillan, A. J. Raman spectra of pyridine adsorbed at a silver electrode. *Chem. Phys. Lett.* **26**, 163–166 (1974).
- Yokota, Y., Ueno, K. & Misawa, H. Essential nanogap effects on surfaceenhanced Raman scattering signals from closely spaced gold nanoparticles. Chem. Commun. 47, 3505–3507 (2011).
- Hu, C. et al. Highly narrow nanogap-containing Au@Au core shell SERS nanoparticles: Size-dependent Raman enhancement and applications in cancer cell imaging. Nanoscale 8, 2090–2096 (2016).
- 16. Mun, C. W. *et al.* Highly sensitive and selective nanogap-enhanced SERS sensing platform. *Nanomaterials* **9**, 619 (2019).
- Li, J. et al. Surface-Enhanced Raman Scattering Active Plasmonic Nanoparticles with Ultrasmall Interior Nanogap for Multiplex Quantitative Detection and Cancer Cell Imaging. Anal. Chem. 88, 7828–7836 (2016).
- 18. Fang, Y., Seong, N. H. & Dlott, D. D. Measurement of the distribution of site enhancements in surface-enhanced raman scattering. *Science (80-.)*. **321**.

- 388-392 (2008).
- 19. Akselrod, G. M. *et al.* Probing the mechanisms of large Purcell enhancement in plasmonic nanoantennas. *Nat. Photonics* 2014 811 **8**, 835–840 (2014).
- 20. Benz, F. *et al.* Nanooptics of molecular-shunted plasmonic nanojunctions. *Nano Lett.* **15**, 669–674 (2015).
- 21. Yi, M. et al. Plasmonic Interaction Between Silver Nano-Cubes and a Silver Ground Plane Studied by Surface-Enhanced Raman Scattering. doi:10.1007/s11468-011-9230-7.
- 22. Marshall, A. R. L. *et al.* Determining molecular orientation: Via single molecule SERS in a plasmonic nano-gap. *Nanoscale* **9**, 17415–17421 (2017).
- Marshall, A. R. L., Roberts, M., Gierschner, J., Bouillard, J.-S. G. & Adawi, A. M.
  Probing the Molecular Orientation of a Single Conjugated Polymer via Nanogap
  SERS. ACS Appl. Polym. Mater. 1, 1175–1180 (2019).
- 24. Li-Jun Wan, †,§, Mimi Terashima, ‡, Hiroyuki Noda, ‡ and & Masatoshi Osawa\*, †. Molecular Orientation and Ordered Structure of Benzenethiol Adsorbed on Gold(111). *J. Phys. Chem. B* **104**, 3563–3569 (2000).
- 25. Moreau, A. *et al.* Controlled-reflectance surfaces with film-coupled colloidal nanoantennas. *Nature* vol. 492 86–89 (2012).
- Dill, T. J., Rozin, M. J., Brown, E. R., Palani, S. & Tao, A. R. Investigating the effect of Ag nanocube polydispersity on gap-mode SERS enhancement factors.
  Analyst 141, 3916–3924 (2016).
- Zeng, Y., Qian, H., Rozin, M. J., Liu, Z. & Tao, A. R. Enhanced Second Harmonic Generation in Double-Resonance Colloidal Metasurfaces. *Adv. Funct. Mater.* 28, 1803019 (2018).
- Rozin, M. J., Rosen, D. A., Dill, T. J. & Tao, A. R. Colloidal metasurfaces displaying near-ideal and tunable light absorbance in the infrared. *Nat. Commun.* 1–7 (2015).
- 29. Jiang, X., Lai, Y., Wang, W., Jiang, W. & Zhan, J. Surface-enhanced Raman spectroscopy detection of polybrominated diphenylethers using a portable Raman spectrometer. *Talanta* **116**, 14–17 (2013).

- Bell, S. E. J. et al. Towards Reliable and Quantitative Surface-Enhanced Raman Scattering (SERS): From Key Parameters to Good Analytical Practice. Angew. Chemie Int. Ed. 59, 5454–5462 (2020).
- 31. Le-The, H. *et al.* Wafer-scale fabrication of high-quality tunable gold nanogap arrays for surface-enhanced Raman scattering. *Nanoscale* **11**, 12152–12160 (2019).
- 32. Biggs, K. B., Camden, J. P., Anker, J. N. & Van Duyne, R. P. Surface-Enhanced Raman Spectroscopy of Benzenethiol Adsorbed from the Gas Phase onto Silver Film over Nanosphere Surfaces: Determination of the Sticking Probability and Detection Limit Time †. *J. Phys. Chem. A* **113**, 4581–4586 (2009).
- 33. Aggarwal, R. L., Farrar, L. W., Diebold, E. D. & Polla, D. L. Measurement of the absolute Raman scattering cross section of the 1584-cm<sup>-1</sup> band of benzenethiol and the surface-enhanced Raman scattering cross section enhancement factor for femtosecond laser-nanostructured substrates. *J. Raman Spectrosc.* 40, 1331–1333 (2009).
- 34. Kukushkin, V. I. *et al.* Metastructures for the Giant Enhancement of Raman Scattering in the Near Infrared Spectral Range. *JETP Lett.* **112**, 31–36 (2020).
- Kubo, A. et al. Nanostructured Assemblies of Gold and Silver Nanoparticles for Plasmon Enhanced Spectroscopy Using Living Biotemplates. Colloids and Interfaces 1, 4 (2017).
- 36. Zhang, Q. *et al.* A metallic molybdenum dioxide with high stability for surface enhanced Raman spectroscopy. *Nat. Commun.* **8**, 1–9 (2017).
- 37. Theiss, J., Pavaskar, P., Echternach, P. M., Muller, R. E. & Cronin, S. B. Plasmonic nanoparticle arrays with nanometer separation for high-performance SERS substrates. *Nano Lett.* **10**, 2749–2754 (2010).
- 38. Alexander, K. D., Skinner, K., Zhang, S., Wei, H. & Lopez, R. Tunable SERS in gold nanorod dimers through strain control on an elastomeric substrate. *Nano Lett.* **10**, 4488–4493 (2010).
- 39. Le Ru, E. C., Meyer, M., Blackie, E. & Etchegoin, P. G. Advanced aspects of electromagnetic SERS enhancement factors at a hot spot. *J. Raman Spectrosc.*

- **39**, 1127–1134 (2008).
- 40. Frey, S. *et al.* Structure of thioaromatic self-assembled monolayers on gold and silver. *Langmuir* **17**, 2408–2415 (2001).
- 41. Wistus, E., Mukhtar, E. & Johansson, L. B. . A conspicuous orientation and localization of pyrene in Langmuir lipid monolayers. *Langmuir* **12**, 3371–3373 (1996).
- 42. Noack, K., Kiefer, J. & Leipertz, A. Concentration-dependent hydrogen-bonding effects on the dimethyl sulfoxide vibrational structure in the presence of water, methanol, and ethanol. *ChemPhysChem* **11**, 630–637 (2010).
- 43. Sahoo, D., Narayanaswami, V., Kay, C. M. & Ryan, R. O. Pyrene excimer fluorescence: A spatially sensitive probe to monitor Lipid-Induced helical rearrangement of apolipophorin III. *Biochemistry* **39**, 6594–6601 (2000).
- 44. Galarneau, A., Lerner, D., Ottaviani, M. F., Di Renzo, F. & Fajula, F. EPR and UV-visible fluorescence spectroscopic evidences for intermediate phases during the formation of micelle-templated silicas. *Stud. Surf. Sci. Catal.* 117, 405–412 (1998).
- 45. Xie, Y. *et al.* Sensing of polycyclic aromatic hydrocarbons with cyclodextrin inclusion complexes on silver nanoparticles by surface-enhanced Raman scattering. *Analyst* **135**, 1389–1394 (2010).
- 46. Saikin, S. K., Olivares-Amaya, R., Rappoport, D., Stopa, M. & Ala'n Aspuru-Guzik, A. On the chemical bonding effects in the Raman response: Benzenethiol adsorbed on silver clusterswz. (2009) doi:10.1039/b906885f.
- Lombardi, J. R., Birke, R. L., Lu, T. & Xu, J. Charge-transfer theory of surface enhanced Raman spectroscopy: Herzberg-Teller contributions. *J. Chem. Phys.* 84, 4174–4180 (1986).
- 48. Valley, N., Greeneltch, N., Van Duyne, R. P. & Schatz, G. C. A look at the origin and magnitude of the chemical contribution to the enhancement mechanism of surface-enhanced Raman spectroscopy (SERS): Theory and experiment. *J. Phys. Chem. Lett.* **4**, 2599–2604 (2013).
- 49. Dill, T. J., Rozin, M. J., Brown, E. R., Palani, S. & Tao, A. R. Investigating the

- effect of Ag nanocube polydispersity on gap-mode SERS enhancement factors. *Analyst* **141**, 3916 (2016).
- 50. Qiu, S. *et al.* Experimental and theoretical study on molecular structure and FT-IR, Raman, NMR spectra of 4,4'-dibromodiphenyl ether. *Spectrochim. Acta Part A Mol. Biomol. Spectrosc.* **76**, 429–434 (2010).
- 51. Schunack, M. *et al.* Long Jumps in the Surface Diffusion of Large Molecules. *Phys. Rev. Lett.* **88**, 156102 (2002).
- 52. Mahaffy, R., Bhatia, R. & Garrison, B. J. Diffusion of a Butanethiolate Molecule on a Au{111} Surface. (1996).
- 53. Sun, Y. & Xia, Y. Shape-controlled synthesis of gold and silver nanoparticles. Science (80-.). 298, 2176–2179 (2002).
- 54. Tao, A., Sinsermsuksakul, P. & Yang, P. Tunable plasmonic lattices of silver nanocrystals. *Nat. Nanotechnol.* **2**, 435–440 (2007).